Which global reanalysis dataset represents better in snow cover on the Tibetan Plateau?

Shirui Yan[1], Wei Pu[1, *], Yang Chen[1], Yaliang Hou[1], Xuejing Li[1], Yuxuan Xing[1],

5   Dongyou Wu[1], Jiecan Cui[2], Yue Zhou[1], Xin Wang[1, *]

[1] Key Laboratory for Semi-Arid Climate Change of the Ministry of Education, College of Atmospheric Sciences, Lanzhou University, Lanzhou 730000, China.

[2] Zhejiang Development & Planning Institute, Hangzhou 310030, China

10

Correspondence to: Wei Pu, (puwei@lzu.edu.cn); Xin Wang, (wxin@lzu.edu.cn)

Abstract. The extensive snow cover across the Tibetan Plateau (TP) regions has a major influence on the climate and water supply for over one billion downstream inhabitants.

15 However, an adequate evaluation of snow cover fraction (SCF) variability over the TP simulated by global multiple reanalysis datasets has yet to be undertaken. In this study, we examined eight global reanalysis SCF datasets using the Snow Property Inversion from Remote Sensing (SPIReS) product spanning the period 2001–2020. The results reveal that the HMASR generated the best SCF simulations because of its outstanding

20 spatial and temporal accuracy. The GLDAS and CFSR demonstrated acceptable SCF accuracy with respect to spatial variability, but struggled to reproduce the annual trend. Pronounced SCF overestimations were found when using the ERA5, ERA5L, and JRA55, but SCF was underestimated by MERRA2, and CRAL generated poor spatial pattern. Overall biases were related to the combined effect of precipitation forcing,

25 temperature forcing, snow data assimilation, and SCF parameterization methods, with the dominant factor changing across datasets. In ERA5 and ERA5L, temperature and snowfall bias exhibited significant correlations with SCF bias over most TP areas, therefore having a greater impact on the accuracy of SCF in terms of spatial variability and temporal evolution. On the other hand, the impact of snow assimilation was

30 possibly more pronounced in MERRA2 and CRAL. Although parameterization methods can improve SCF simulation accuracy, their influence was weaker than those of other factors, except for JRA55. To further improve the accuracy of SCF simulation, an ensemble average method was developed. The ensemble based on HMASR and GLDAS generated the most accurate SCF spatial distribution, whereas the ensemble

35 containing ERA5L, CFSR, CRAL, GLDAS, ERA5, and MERRA2 proved optimal for capturing the annual trend.

Keywords

Snow cover; Tibetan Plateau; Reanalysis dataset; Meteorological forcing factors; Data assimilation; Parameterization methods

1 Introduction

40

Widespread snow cover on the Tibetan Plateau (TP), with its high albedo and low thermal conductivity, plays a crucial role in the surface energy balance (Zhang, 2005) and affects the climate both locally (Zhang et al., 2022) and across Asia and globally (Lyu et al., 2018; Ma et al., 2017). Furthermore, in its role as the "Asian water tower"

45 (Kitoh and Arakawa, 2016; Qiu, 2008; Xu et al., 2008), the snow that accumulates on the TP during the cold season is an essential freshwater resource for over a billion people during the warm season, supplying their domestic, agricultural, and industrial water needs (Immerzeel et al., 2010). In the context of global warming, the snow cover over the TP shows high variability and acts as an extremely sensitive indicator of

50 climate change (Dawson et al., 2016). Therefore, the accurate and reliable representation of snow cover over the TP is crucial to climate and ecosystem studies. Ground-based measurements are the most accurate observations with respect to snow cover. However, the complex terrain and harsh weather conditions on the TP present challenges to comprehensive monitoring (Beniston et al., 2018), leading to issues of

55 spatial representativeness. In contrast, optical satellite observations provide global-scale snow cover data and offer crucial support for snow research. For example, NASA's Moderate Resolution Imaging Spectroradiometer (MODIS) has been providing moderate-resolution global daily snow cover fraction (SCF) data since 2000 (Hall et al., 2002). Based on these observations, the Snow Property Inversion from

60 Remote Sensing (SPIReS) product uses a more advanced spectral decomposition method and further considers the impacts of light-absorbing particles on snow reflectance, and is recognized as the most accurate optical remotely sensed snow cover product (Stillinger et al., 2023). However, the time period covered by satellite remote sensing data is relatively short, which limits their utility for long-term climate analysis.

65 Reanalysis methods based on observations and mathematical models provide a critical avenue for obtaining long-term snow data. These techniques use data assimilation to

integrate historical environmental observations with short-term weather forecasts, yielding optimal estimates of global or regional weather and climate states (Lei et al., 2023). In recent decades, the major global meteorological agencies have generated

70 atmospheric and land reanalysis products at varying temporal and spatial resolutions. Reanalysis datasets have become indispensable sources of data when it comes to studying processes related to snow variability, as well as their impacts and responses to climate change. The reanalysis snow dataset has revealed that anomalous snow cover facilitates a warm-north, cold-south winter over North America by influencing the

75 teleconnection response in the Pacific-North American (PNA) region (Lin and Wu, 2011). Reanalysis datasets have been integrated into the Canadian Sea Ice and Snow Evolution (CanSISE) dataset to analyze the impacts of global warming on snow changes on the TP (You et al., 2020a).

A comprehensive evaluation of multiple snow reanalysis datasets based on referenced

80 observation data is of paramount importance before launching related scientific research. Previous research has devoted considerable attention to evaluating Snow Depth (SD) and Snow Water Equivalent (SWE) reanalysis datasets using various metrics from different regions (Bian et al., 2019; Li et al., 2022; Wang and Zeng, 2012). However, only a few studies have assessed SCF over the TP calculated using reanalysis

85 datasets based on the Interactive Multisensor Snow and Ice Mapping System (IMS; Helfrich et al., 2007) satellite and ground data (Li et al., 2022; Orsolini et al., 2019). These studies have provided comparisons of the SCF spatial patterns among a limited number of reanalysis datasets, yet they lack comprehensive multidimensional analysis that considers aspects such as regional variations and temporal trends (Li et al., 2022;

90 Orsolini et al., 2019). In addition, the IMS dataset, which uses microwave remote sensing technology, contains significant variations in the brightness temperature of wet snow that lead to increased uncertainty in snow cover detection (Yu et al., 2013). More importantly, these studies have not conducted a thorough exploration of the underlying

reasons for the biases associated with the reanalysis datasets.

95   The various reanalysis snow datasets have unique spatiotemporal characteristics (Mudryk et al., 2015). The differences in snow characteristics originate not only from the use of different Land Surface Models (LSMs), but also from the meteorological forcing data and post-optimization via snow data assimilation. De Rosnay et al. (2014) indicated that the accuracy of snow simulations is constrained largely by uncertainties

100   associated with some of the key meteorological inputs, including precipitation and temperature (Zhang et al., 2015), under regional climate conditions and elevation factors (Brown and Mote, 2009; Hernández-Henríquez et al., 2015). Therefore, uncertainties associated with precipitation and temperature data are likely to be the primary sources of bias within the reanalysis SCF datasets. Moreover, Jiang et al. (2020)

105   emphasized that optimizing the parameterization methods for SCF calculation would significantly reduce the uncertainties associated with snow modeling, which would further reduce biases in land surface albedo simulations, particularly in high-altitude regions. The reanalysis datasets use different SCF parameterization methods, with a 100% SCF corresponding to an SD that ranges from 26 to 2 cm (Orsolini et al., 2019).

110   The selection of different SCF parameterizations for the reanalysis datasets may lead to varying degrees of SCF bias. On the other hand, data assimilation represents an effective approach to reducing the uncertainties in snow models and enhancing the ability to monitor seasonal snow changes (Andreadis and Lettenmaier, 2006; Sun et al., 2004). Brown et al. (2003) used optimal interpolation (OI) techniques to assimilate SD

115   observations, resulting in gridded monthly SD and SWE datasets that were better aligned with in situ and satellite data across North America.

For this study, we used the SPIReS remote sensing product as the reference dataset to conduct an in-depth evaluation of SCF simulations derived from eight global atmospheric and land assimilation reanalysis datasets over the period 2001–2020. The

120   accuracy of SCF was assessed multidimensionally by examining the spatial

characteristics, seasonal variations, and temporal trends across the whole TP and its nine basins. Additionally, we aimed to assess the influence of meteorological forcing factors (snowfall and temperature), snow assimilation, and the SCF parameterization method on the biases associated with the various reanalysis SCF datasets. On this basis,

125 we attempted to develop an optimal ensemble of reanalysis SCF datasets, and provide a useful guide for the research community regarding climatic and cryospheric changes over the TP.

2 Data and methods

2.1 Data

130 #### 2.1.1 Remote sensing product

For this study, we used the SPIReS (Bair et al., 2021) product as the reference dataset for SCF. SPIReS is derived from Landsat 8 Operational Land Imager (OLI) and Moderate-Resolution Imaging Spectroradiometer (MODIS) data using a spectral unmixing methodology. The SCF calculation in SPIReS relies on two endmembers (i.e.,

135 snow and snow-free) along with an ideal shade component, effectively simplifying the calculation process while maintaining high accuracy. SPIReS reduces the effects of data and cloud noise through interpolation and smoothing to provide more accurate SCF data (Bair et al., 2021; Dozier et al., 2008). Validation of SPIReS was conducted by Stillinger et al. (2023) using airborne lidar datasets, and they reported that SPIReS has

140 reduced biases (–0.1%) and a lower root mean square error (RMSE; 12.0%) when compared with the band ratio approaches applied to MODIS data.

2.1.2 Reanalysis datasets

We examined eight reanalysis datasets obtained from various global meteorological organizations. Meteorological forcing fields are used to drive the LSMs, and

145   parameterization methods are used to calculate the daily SCF data; however, the assimilation of the snow data differed among the datasets (Table 1).

The High Mountain Asia Snow Reanalysis (HMASR; Liu et al., 2021) is a snowpack-specific reanalysis dataset produced by the recent NASA High Mountain Asia Team (HiMAT). HMASR uses the Simplified Simple Biosphere model, version 3 (SSiB3;

150   Sun and Xue, 2001; Xue et al., 2003) as the LSM to generate the initial snowpack mass based on meteorological inputs from MERRA2 and physiographic characteristics. The model-derived SCF predictions are then constrained by integrating SCF data from the Landsat satellites and MODIS Snowpack Area and Grain Size (MODSCAG; Painter et al., 2009) products via data assimilation. The parameterization method used in HMASR

155   (abbreviated as SSiB3_SCF) has not been publicly disclosed. HMASR covers the period from October 2000 to September 2017, but our analysis focused on the period 2001 to 2016 to exclude the incomplete start/end years.

The Modern-Era Retrospective analysis for Research and Applications, version 2 (MERRA2; Gelaro et al., 2017) dataset, developed by NASA's Global Modeling and

160   Assimilation Office (GMAO), provides land surface state estimates including SCF via the Catchment Land Surface Model (CLSM; Koster et al., 2000). The surface-forced precipitation is a combination of the National Oceanic and Atmospheric Administration (NOAA) Climate Prediction Center (CPC) unified gauge-based analysis of global daily precipitation (CPCU; Xie et al., 2007) product and the precipitation generated by the

165   atmospheric general circulation model (AGCM) within the MERRA2 system. The generated precipitation is also adjusted using a precipitation correction algorithm (Reichle et al., 2017). However, it is important to note that MERRA2 does not include snow data assimilation. The parameterization scheme in MERRA2 considers 100% SCF to occur when the SWE reaches a threshold of 26 kg m^{-2} (abbreviated as

170   MM_SCF).

The ECMWF Reanalysis version 5 (ERA5; Hersbach et al., 2020), produced and

published by the European Centre for Medium-Range Weather Forecasts (ECMWF), uses the Tiled ECMWF Scheme for Surface Exchanges over Land (HTESSE) model to simulate various land surface variables including SCF. The precipitation forcing in

175 ERA5 is adjusted using Global Precipitation Climatology Project (GPCP; Adler et al., 2003) data. ERA5 assimilates in situ SD observations and binary snow cover data from IMS only below 1500 m, so that snow assimilation does not apply to the TP region (Bian et al., 2019). Additionally, a refined dataset known as ERA5-Land (abbreviated as ERAL; Muñoz-Sabater et al., 2021) has been derived from ERA5 via the offline

180 rerunning of the land portion of the model at a higher spatial resolution. ERA5L provides solely land surface parameters and is based on the same forcing and LSM as ERA5. Both datasets have a 10-cm SD threshold to identify full snow cover (abbreviated as ME_SCF).

The Japanese 55-year Reanalysis (JRA55; Fujiwara et al., 2017), developed by the

185 Japan Meteorological Agency (JMA), generates the land surface analysis field using an offline version of the Simple Biosphere (SIB) model (Sato et al., 1989; Sellers et al., 1986). The precipitation forcing is corrected using precipitable water retrieved from the Special Sensor Microwave/Imager (SSM/I) brightness temperature (Onogi et al., 2007). JRA55 incorporates daily SD data from the SSM/I and the Special Sensor Microwave

190 Imager Sounder (SSMIS) using a univariate two-dimensional OI approach. In addition, it assimilates surface synoptic observations (SYNOP) reports and digitizes China's daily SD data from 1971 to 2006 (Onogi et al., 2007). The detection of full snow cover in JRA55 is based on a 2-cm SD threshold (abbreviated as MJ_SCF).

The Climate Forecast System Reanalysis (CFSR; Saha et al., 2010), developed by the

195 National Center for Environmental Prediction (NCEP) under NOAA, is a weakly coupled global reanalysis system. The land surface analysis utilizes the Noah model (Meng et al., 2012). Two observed global precipitation analyses, namely the CPC Merged Analysis of Precipitation (CMAP; Xie and Arkin, 1997) and the CPCU, are

used as alternative forcings for precipitation. In terms of snow analysis, CFSR

200 assimilates IMS and the Global Snow Depth Model (SNODEP). On 1 January 2011, CFSR transitioned to a newer version of the NCEP data assimilation system called CFSv2 (Saha et al., 2014). Despite differences in horizontal resolution and minor changes to the physical parameterization, CFSv2 is considered a continuation of CFSR in most cases (Fujiwara et al., 2017). However, the inherent discontinuities in this

205 dataset may introduce changes in boundary conditions, potentially leading to variations in model output variables (Fujiwara et al., 2017). Consequently, we examined the entire temporal domain of CFSR (Fig. S1). We found noticeable uncontrollable oscillatory patterns in SCF, snowfall, and temperature during the period 2007-2010, which were therefore excluded from our subsequent assessments. The SCF parameterization

210 method in CFSR is related to the surface characteristics, using varying SD thresholds to identify the full SCF depending on the underlying surface type (abbreviated as Noah_SCF).

The Global Land Data Assimilation System version 2.1 (GLDAS-2.1; Rodell et al., 2004) is a global land data assimilation product developed jointly by NASA and NOAA.

215 It uses the global meteorological forcing dataset from Princeton University (Sheffield et al., 2006) and the GPCP V1.3 Daily Analysis precipitation fields (Adler et al., 2003; Huffman et al., 2001) to drive three distinct LSMs: the CLSM model, the Noah model, and the Variable Infiltration Capacity (VIC) model. As a result, four datasets are generated (Table S1). Notably, the full series datasets within GLDAS-2.1 do not

220 assimilate snow observations. Furthermore, owing to the unavailability of SCF variables in these datasets, this study derived different SCF values using three parameterization methods (MM_SCF, ME_SCF and MJ_SCF). Finally, the $0.25° \times 0.25°$ GLDAS–Noah product using the MM_SCF approach was selected as a representative of GLDAS due to its better SCF simulation (Fig. S2).

225 CRA-Land (CRAL; Liu et al., 2023) is the land surface component of the first

generation of China's global reanalysis dataset produced by the China Meteorological Administration (CMA). CRAL uses an updated version of the Noah model. The precipitation meteorological forcing is derived from a similar combination of data sources as CFSR (Liang et al., 2020). However, CRAL does not assimilate other

230   observational data in the LSM. Instead, data from over 2,400 CMA surface weather observatories indirectly influence the land surface product through conventional meteorological forcing derived from atmospheric reanalysis (Liang et al., 2020). The SCF parameterization method in CRAL is the same as that in CFSR.

235   **Table 1: Characteristics of the reanalysis datasets used in this study.**

Reanalysis dataset	Centre	Temporal coverage	Resolution	Land Model	Snow data assimilation	Variables used in analysis	SCF parameterization Scheme
HMASR	NASA HIMAT	1999 to 2017	1/225°×1/225°	SSiB3	Landsat and MODSCAG	SCF	SSiB3_SCF
MERRA2	NASA GMAO	1980 to present	0.625°×0.5°	Catchment	-	SCF, SWE, SD, Snowfall, T2	SCF= min (1, SWE/26) *
ERA5	ECMWF	1979 to present	0.25°×0.25°	H-TESSEL	-	SCF, SWE, SD, Snowfall, T2	SCF= min (1, (SD)/10) *
ERA5-Land	ECMWF	1981 to present	0.1°×0.1°	H-TESSEL	-	SCF, SWE, SD, Snowfall, T2	SCF= min (1, (SD)/10) *
CRA-Land	CMA	1979 to present	0.5°×0.5°	Noah	-	SCF, SWE, SD, Snowfall, T2	Noah_SCF
JRA55	JMA	1958 to present	0.563°×0.563°	SiB	Station, SSM/I, SSMIS	SCF, SWE, SD, Snowfall, T2	SCF= min (1, (SD)/2) *
CFSR / CFSv2	NOAA NCEP	1979 to present	0.5°×0.5°	Noah	SNODEP, IMS	SCF, SWE, SD, Snowfall, T2	Noah_SCF
GLDAS	NASA and NOAA	2000 to present	0.25°×0.25°	Noah	-	SWE, SD, Snowfall, T2	Noah_SCF

* The unit for SWE is kg m^{-2}, and for SD is cm.

2.1.3 Meteorological dataset

To identify the source of the SCF bias, we used the high-resolution near-surface meteorological forcing dataset for the Third Pole region (TPMFD; Yang et al., 2023) as

240   the reference dataset. Precipitation and 2-m temperature are derived by combining a short-term high-resolution Weather Research and Forecasting (WRF) simulation (Zhou

et al., 2021), long-term ERA5 data, and in situ observations. The precipitation data are downscaled using a Convolutional Neural Network (CNN) trained on WRF simulations. Validation conducted by Jiang et al. (2023) demonstrates that the precipitation data from

245 TPMFD are unbiased overall and considerably better than other widely used datasets, including the latest generation of reanalysis (ERA5L), a state-of-the-art satellite-based dataset (IMERG), and multi-source merged datasets (MSWEP v2 and AERA5-Asia).

2.2 Methods

We used bias and Pearson's correlation coefficient (R) as the principal metrics to

250 evaluate the accuracy of the SCF across different reanalysis datasets. The assessment of SCF accuracy in relation to spatial and temporal variations was obtained by calculating spatial correlations and comparing temporal trends. To capture the spatial correlation from various perspectives and levels, we used Taylor diagrams (Taylor, 2001) to visually represent the combined information of standard deviation ratio

255 (STDR), central RMSE, and spatial correlation coefficients. STDR quantifies the degree of similarity in the dispersion patterns between the reanalysis dataset and observational data. Additionally, Taylor skill scores (SS, ranging from 0 to 1; Taylor, 2001) were calculated to provide comprehensive statistics for the composite index. The SS is defined as follows:

260 $$SS = \frac{4(1+R)^4}{(STDR + 1/STDR)^2 (1+R_0)^4} \tag{1}$$

where R_0 is the maximum correlation attainable.

The reliability of trend analysis depends on the significance testing, and the sign (+ or –) may impact the robustness of the trend analysis results. Therefore, we used the Mann–Kendall (MK; Kendall, 1975; Mann, 1945) test to ascertain the significance of

265 temporal trends, and the consistency index (CI; Zhang et al., 2021) to validate the SCF trends. The CI is defined as follows:

$$CI = \frac{N_{inc} + N_{dec} + N_{no}}{N_{tot}} \qquad (2)$$

where N_{inc} is the number of grid points with a significant increasing trend in both the reanalysis dataset and SPIReS (P < 0.05), N_{dec} is the number of grid points with a

270   significant decreasing trend in both datasets, N_{no} is the number of grid points with a non-significant trend in both datasets, and N_{tot} is the total number of grid points. The higher the CI value, the better the performance of the trend simulation.

3. Results

3.1 Spatial variability of SCF climatology

275   **3.1.1 Evaluation of spatial variability**

The reanalysis datasets exhibit a range of snow cover patterns over the TP (Fig. 1a). The basin-averaged values were obtained by averaging pixel points within each basin of the TP throughout the dataset from 2001 to 2020 (Fig. 1b). The regional average SCF values from HMASR, GLDAS, and CRAL are 0.14, 0.12, and 0.11, respectively, which

280   align closely with the SPIReS average value of 0.13. In more detail, HMASR (GLDAS and CRAL) displays a slight underestimation (overestimation) in westerlies-dominated basins such as the Amu Darya and Indus, and overestimation (underestimation) in monsoon-dominated basins such as the Yellow, Yangtze, Mekong, Salween, and Brahmaputra (Fig. 2a). This indicates a more accurate SCF simulation. On the other

285   hand, ERA5, ERA5L, and JRA55 show large positive biases in SCF across all basins, whereas MERRA2 displays a large negative bias in SCF. ERA5 and MERRA2 yield the least-accurate SCF values for the whole TP, with extreme regional averages of 0.41 and 0.05, respectively, which are highly different from the SPIReS satellite observations. Figure 1a and 2a further show that, although all reanalysis datasets have spatial SCF

290   patterns that are similar to those from SPIReS, the varying magnitude of SCF across

these datasets results in different spatial correlations (characterized by R values) and similarities in dispersion patterns (characterized by STDR values) when compared with SPIReS, which ultimately influences their synthesis performance (characterized by SS values). In the Taylor diagram (Fig. 2b; see Fig. S3 for a clearer version), HMASR has

295   the highest R values across all basins, with STDR values for monsoon-dominated basins close to 1 (e.g., 0.96 for the Yangtze River). Consequently, HMASR achieves the highest SS value of 0.67, indicating its superior SCF performance across the whole TP. Although GLDAS has slightly lower R values than HMASR in the westerlies-dominated basins (Amu Darya and Indus) and inland basins (Tarim and Inner Tibetan

300   Plateau), its STDR values are closer to 1. This enables GLDAS to perform as well as HMASR over the whole TP, as characterized by the same highest SS value. CFSR consistently exhibits high R values across all basins, despite its moderate performance in the regional climate averages. Consequently, CFSR has an SS value of 0.62, second only to HMASR and GLDAS. In contrast to CFSR, although CRAL has a regional

305   average SCF close to SPIReS, its spatial distribution is overly uniform, with a relatively low spatial correlation, leading to a moderate SS value. The Taylor performance of ERA5 is notably poor, which corresponds to its extreme regional average. Bian et al. (2019) also reported the inadequate performance of ERA5 in representing snow-related characteristics, with the highest RMSD values and the lowest R value. MERRA2 shows

310   the worst Taylor performance, not only across the whole TP but also within each basin. This seems opposite to the conclusions of Orsolini et al. (2019), who found MERRA2 to perform well in capturing the SCF and SWE characteristics on the TP. The reason for this discrepancy is that their results depended mainly on the high spatial correlation between MERRA2 and the reference dataset, while overlooking the severe

315   underestimations in SCF values. These underestimations result in a very small self-standard-deviation in the STDR calculation, leading to the worst SS value in this study of 0.2.
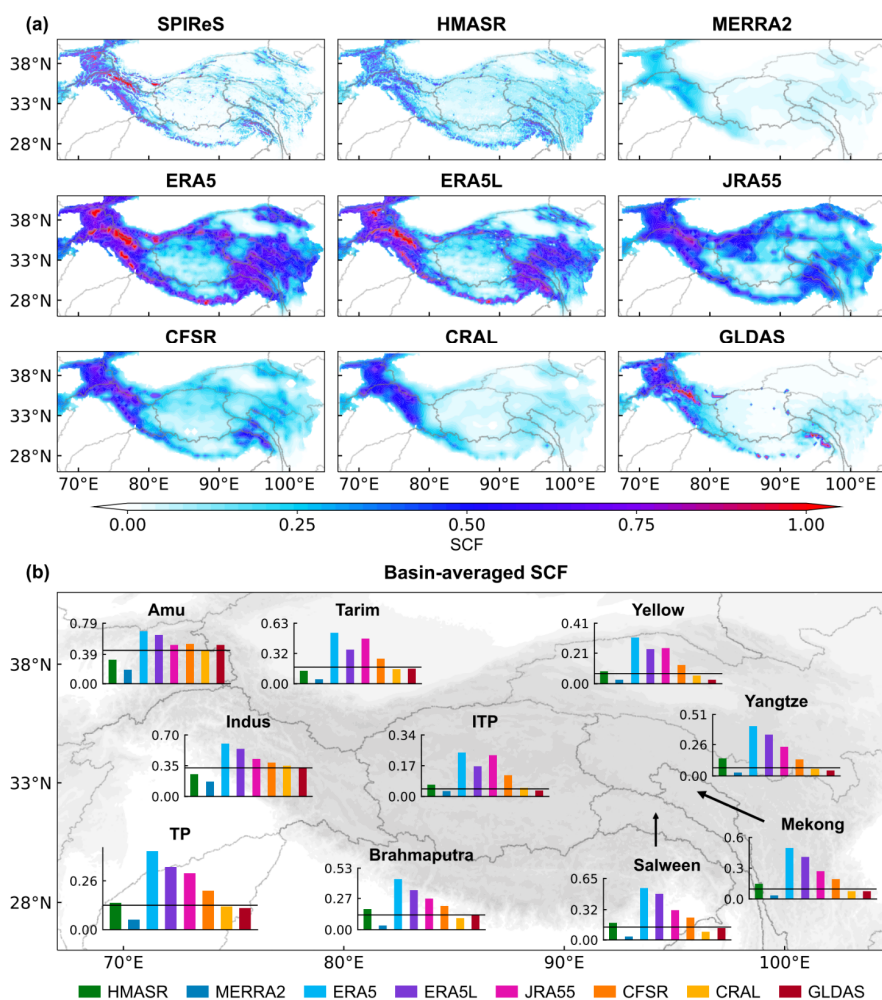
Figure 1: (a) Spatial distribution of average Snow Cover Fraction (SCF) for 2001–2020 over the Tibetan Plateau region. (b) Basin-averaged SCF for 2001–2020 from SPIReS (black horizontal line) and the eight reanalysis datasets overlain on a map of the Tibetan Plateau region. ITP = Inner Tibetan Plateau.

For each reanalysis dataset, the SCF simulation exhibits varying performance over different TP basins, influenced by their unique topographic and climatic characteristics. Basins affected primarily by the winter westerlies (e.g., the Amu Darya and Indus basins) display better consistency between reanalysis datasets and SPIReS. The Indus basin shows the best performance in the SCF regional average and the highest SS value.

In basins influenced by the summer monsoon (e.g., the Yellow, Yangtze, Mekong, Salween, and Brahmaputra basins) the SCF performance varies. All reanalysis datasets

330 are scattered on the Taylor diagram panels in monsoon-dominated basins except for the Salween. In particular, ERA5, ERA5L, and JRA55 (MERRA2) produce regional averages more than 2× larger (lower) than SPIReS. In the inland basins (e.g., the Tarim and Inner Tibetan Plateau basins) most reanalysis datasets exhibit greater deviations compared with other basins. ERA5, JRA55, CRAL, and MERRA2 have much lower

335 SS values (<0.15), reflecting the poorest performance in these basins.
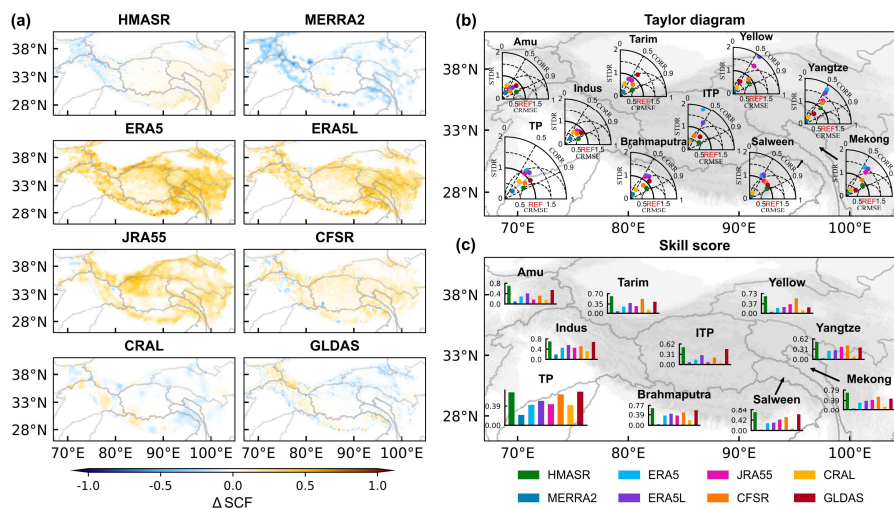
Figure 2: (a) Spatial distribution of the average SCF bias from the reanalysis datasets based on SPIReS for 2001–2020 over the Tibetan Plateau region. (b)
340 **Taylor diagrams showing the spatial correlation coefficients (R) and standard deviation ratio (STDR) of SCF between reanalysis datasets and SPIReS for each basin, overlain on a map of the Tibetan Plateau region. (c) Taylor skill scores (SS) for each basin overlain on a map of the Tibetan Plateau region.**

3.1.2 Bias attribution in the spatial distribution of SCF

345 The evolution of SCF can be determined from the balance between snow mass gain via snowfall and snow depletion via snowmelt, sublimation, and wind drifting (Liu et al.,

2022), as well as from the data assimilation techniques used in the reanalysis datasets. Our findings demonstrate that reanalysis datasets incorporating snow assimilation (e.g., HMASR and CFSR) always outperform those without snow assimilation, including

350   ERA5, ERA5L, MERRA2, and CRAL, across the whole TP and for all of its basins, in terms of SCF regional averages and SS values. Moreover, HMASR (MERRA2 and CRAL) with (without) snow assimilation showed a better (worse) performance with respect to the SCF annual trends (see Section 3.2.2). This highlights the effectiveness of snow assimilation in enhancing the accuracy of SCF simulation. Indeed, previous

355   studies have indicated that advanced data assimilation algorithms, which use multiple observational datasets to interpolate and correct the initial or output model values and so constrain the discrepancies between models and observations, can improve the accuracy and reliability of numerical models (Reichle, 2008). For instance, Magnusson et al. (2017) used a particle filter method to assimilate SD observations into a multilayer

360   energy-balance snow model, resulting in reduced errors in SWE, snowpack runoff, and soil temperature. However, there were two unexpected results regarding the JRA55 and GLDAS datasets. First, GLDAS, despite lacking snow data assimilation, ranks second in SCF simulation performance among all datasets. Conversely, JRA55, which incorporates daily SD data from SSM/I and SSMIS, as well as surface synoptic

365   observations, performs less well than half of the reanalysis datasets that do not incorporate snow assimilation. These results imply that other factors influence the accuracy of the SCF simulation. Variations in snowfall and temperature are the dominant influence on snow evolution and can explain half to two-thirds of the interannual variability in snow cover (Xu et al., 2017). Hence, the accuracy of these

370   two pivotal meteorological forcing factors directly impacts the integrity of the LSMs (Zhang et al., 2015). In addition, different SCF parameterizations influence the instability inherent in the snow models (Dutra et al., 2011). Therefore, we further investigated the SCF bias by examining the performance with respect to snowfall and

temperature in each reanalysis dataset, along with the inadequacies of parameterization

375   methods.
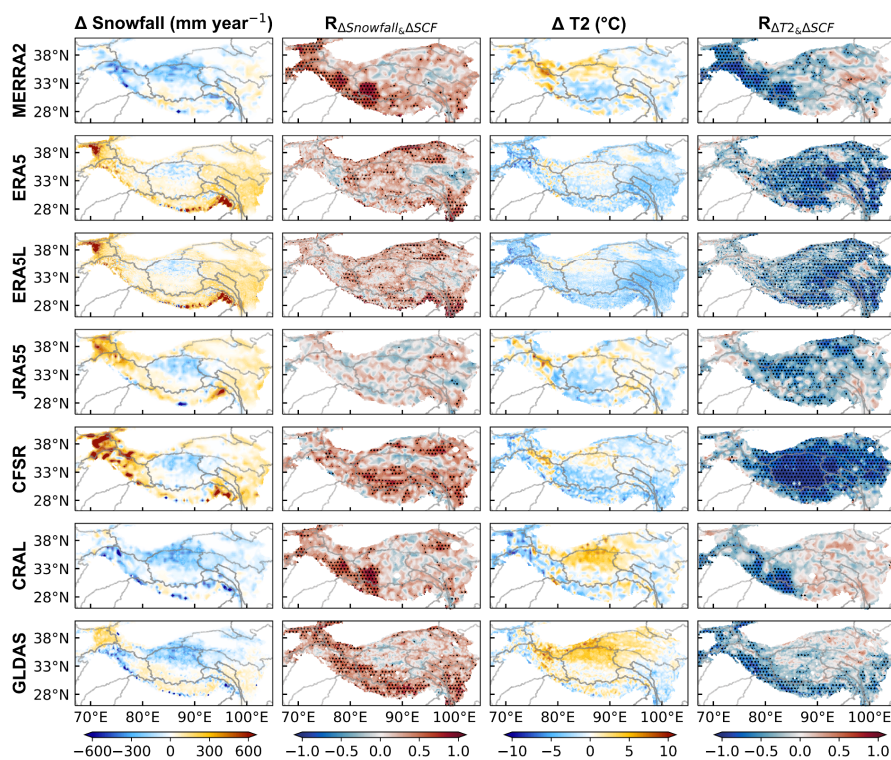
Figure 3: The columns show (from left to right): spatial distribution of the averaged snowfall bias from the reanalysis datasets based on TPMFD for 2001–2020 over the Tibetan Plateau region; spatial distribution of the correlation coefficients (R value) between snowfall bias and SCF bias; spatial distribution of the averaged 2-m temperature (T2) bias for 2001–2020; and spatial distribution of R values between T2 bias and SCF bias. Black dots in the second and fourth columns indicate that the correlation exceeds the 95% confidence level.

ERA5, ERA5L, and CFSR overestimated snowfall in both the westerlies-dominated

385   and monsoon-dominated basins (Fig. 3). The snowfall biases are particularly

pronounced in the western and southeastern regions of the TP, including on the Pamir

Plateau and the southern slopes of Mount Namcha Barwa. The only exception is the

inland basin of the Inner Tibetan Plateau, where snowfall is underestimated. In contrast

to snowfall, these reanalysis datasets consistently underestimated temperatures in

390   westerlies-dominated and monsoon-dominated basins. The excessive snowfall

contributes to heightened snow accumulation, while the reduced temperatures hinder

the ablation process by impeding the snow from attaining the freezing threshold (Liu et

al., 2022). Simultaneously, under conditions of adequate atmospheric water vapor, low

temperatures further intensify snow accumulation through enhanced snowfall (You et

395   al., 2020b). The combined impacts result in a positive SCF bias within ERA5, ERA5L,

and CFSR, characterized by significant correlations between snowfall and temperature

bias versus SCF bias. Moreover, compared with snowfall, temperature bias exhibits

stronger significant correlations with SCF bias over broader areas. This implies that

physical processes influenced by temperature bias may have a more pronounced and

400   widespread responsibility with respect to SCF bias. JRA55 shows a similar pattern of

snowfall and temperature bias to ERA5, ERA5L, and CFSR, but these two

meteorological factors can explain SCF in only limited areas. In addition, because

JRA55 incorporates multiple snow observations, the snow assimilation cannot be the

primary cause of the SCF bias. This suggests the presence of another significant factor

405   that is responsible for the overestimation of SCF in JRA55. A previous study indicated

that JRA55 performed well with respect to SD simulation and benefited from the

assimilation of SD data from Chinese ground observation stations (Orsolini et al., 2019).

This indirectly implies the influence of the SCF parameterization method. Indeed,

JRA55 uses an aggressive parameterization approach with a 2-cm SD threshold to

410   define the complete SCF, which differs markedly from other reanalysis datasets (see

Section 2.1.2). When adopting a more appropriate parameterization method (see Fig.

9), the SCF simulation by JRA55 shows a noteworthy increase in the SS value of 0.12.

This apparent improvement confirms the important role of the parameterization method

in influencing SCF accuracy in JRA55. For MERRA2 and CRAL, the snowfall and

415   temperature bias can explain the SCF bias over only a limited area of the TP. In addition,

alternative SCF parameterization methods are unable to improve the SCF simulation. Therefore, we propose that the absence of snow assimilation, which is used to correct the LSM-derived initial snowpack, is the main reason for the SCF bias in MERRA2 and CRAL. Interestingly, regardless of the snow assimilation or SCF parameterization

420 methods, most of the reanalysis datasets show significant correlations between the bias in snowfall and temperature versus SCF in high-altitude areas above 5 km, such as the Karakoram Mountains, Pamir Plateau, and Himalaya, which suggests a primary contribution of snowfall and temperature to SCF bias in these regions.

3.2 Seasonal evolution and annual trends in SCF

425 **3.2.1 Evaluation of seasonal evolution and bias attribution**

Figure 4 shows the SCF bias, its probability density distribution, and the skill scores for the four seasons. In general, the different seasons show similar spatial patterns of SCF bias for each reanalysis dataset, which is consistent with the annual average results. This suggests the persistent influence of the uncertainties associated with the snowfall

430 and temperature data, on the SCF bias throughout the year. However, the bias values vary seasonally, with higher biases observed during the accumulation period (winter and spring), but lower biases during the ablation period (summer and autumn). The largest bias in winter can be several times larger than the lowest bias in summer. However, this does not imply a better SCF simulation for summer than winter. As the

435 SCF during winter is much higher than that during summer (Fig. S4), a smaller fractional difference in winter can result in a larger absolute bias. Conversely, the spatial correlations and similarity in dispersion patterns between the reanalysis datasets and SPIReS SCF are higher during the accumulation period than the ablation period, leading to a better Taylor performance for winter and spring, as shown by the larger SS values.

440 The seasonal variability associated with the SCF simulation performance is most evident in MERRA2 and CRAL.
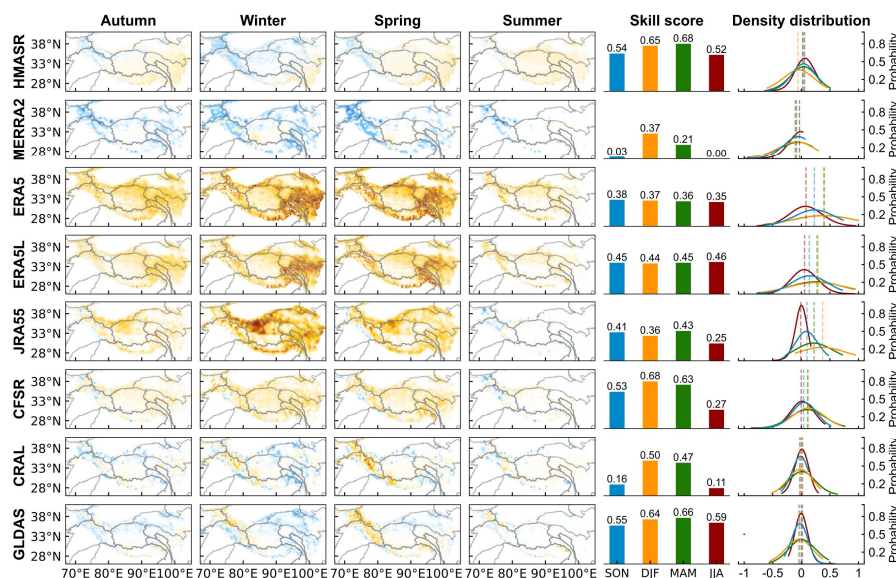
Figure 4: The first four columns show the spatial distribution of seasonal SCF bias from the reanalysis datasets based on SPIReS over the Tibetan Plateau region during (left to right): autumn (September–November: SON), winter (December–February: DJF), spring (March–May: MAM), and summer (June–August: JJA). The SS values are shown in the fifth column. The probability density distribution of SCF bias is shown in the sixth column. The dashed lines in the sixth column represent the TP-average SCF bias for each season.

Figure 5 further shows the seasonal evolution of the SCF bias, as well as the snowfall and temperature biases. For the four reanalysis datasets, including ERA5, ERA5L, JRA55, and CFSR, snowfall (temperature) shows large positive (negative) biases during the accumulation period, which together cause the large positive SCF bias during winter and spring. In contrast, both the snowfall and temperature biases are small during the ablation period, resulting in a small SCF bias. Thus, snowfall and temperature collectively explain the apparent seasonal variations in the SCF bias, as evidenced by the statistically significant correlations. Compared with snowfall, the temperature bias seems to have a greater impact, which is characterized by the larger R values. For MERRA2, CRAL, and GLDAS, the SCF biases remain small and stable across all four seasons, which corresponds to the well-simulated snowfall, despite the highly variable

temperature bias. Therefore, snowfall may be more responsible for the seasonality in the SCF bias associated with these three reanalysis datasets.
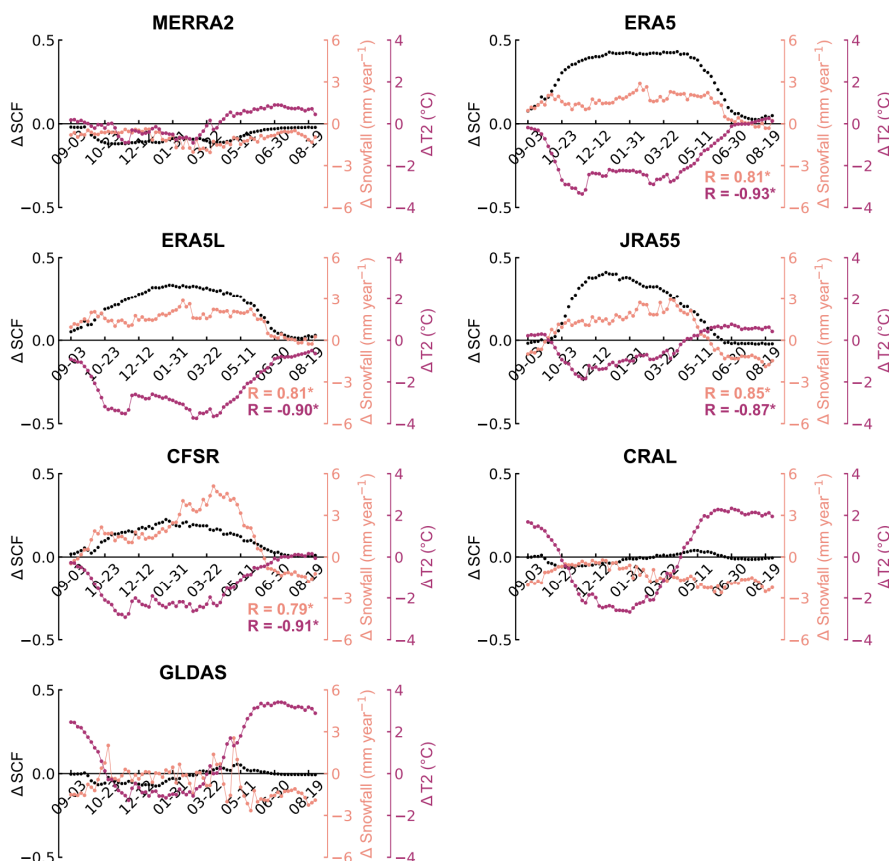
Figure 5: Temporal variations of SCF (black), snowfall (light pink), and T2 (purple) bias averaged at five-day intervals from all reanalysis datasets. R in light pink (purple) represents the correlation coefficient between snowfall (T2) bias and SCF bias. The stars indicate the correlation exceeds the 95% confidence level.

3.2.2 Evaluation of annual trends and bias attribution

Figure 6 presents the annual trends in SCF from 2001 to 2020 for the SPIReS and seven reanalysis datasets. As HMASR covers only the period from 2001 to 2016, a separate comparison between HMASR and SPIReS is provided in Fig. S5. The SPIReS satellite observations generally show increased SCF over the Indus, west Brahmaputra, Yellow,

Yangtze, and Mekong basins, but decreased SCF over the Amu Darya, Tarim, and east Brahmaputra basins. However, these trends are not statistically significant over most

475   areas of the TP, indicating fluctuations in the variability of SCF over the past two decades. This pattern is clearly demonstrated by the spatial distribution of snowfall and temperature trends (Fig. 8). In comparison to SPIReS, ERA5L and ERA5 show greater variability in the SCF trends, especially in the Tarim basin and on the southeastern TP, where a significant decrease in SCF is evident. Nevertheless, ERA5L and ERA5 still

480   exhibit the most similar spatial patterns to SPIReS, with the highest R values. Moreover, ERA5L and ERA5 have the highest CI values (>0.5) over the whole TP and in most basins (Fig. 7), indicating that these datasets can reproduce the SCF trend over more than half of the area of the TP. Consequently, ERA5L and ERA5 demonstrate the best performance in SCF trend simulation among these eight reanalysis datasets. This can

485   be attributed to the superior spatial consistency of ERA5L and ERA5 when compared with TPMFD with respect to simulations of snowfall and temperature trends (Fig. 8).
      The SCF trend simulated using the HMASR data is also accurate, with a spatial pattern similar to SPIReS, and high CI values of around 0.5 over the TP and all basins (Fig. S5). Therefore, the performance of HMASR is very close to that of ERA5L and ERA5.

490   Combining the analysis in Section 3.1, we note that HMASR is the best reanalysis dataset for SCF simulation based on its outstanding performance in both the spatial and temporal dimensions. This is because HMASR directly assimilates snow cover data, not only from the moderate-resolution MODIS satellite, but also from the high-resolution Landsat satellite. The high-resolution data improve the SCF spatial

495   simulation, while the medium-resolution data enhance the temporal simulation. Moreover, the MODSCAG algorithm-based satellite SCF products assimilated by HMASR are more accurate than the NDSI-based SCF. Previous studies also reported the superior SWE simulation generated using the HMASR data when compared with the other seven reanalysis datasets over the TP (Liu et al., 2022). MERRA2 shows a

22

500   general increasing trend for SCF, which is statistically significant over approximately

half of the TP. This is caused mainly by the widespread and significant increase in

snowfall simulation (Fig. 8). This spatial pattern in the SCF trends differs considerably

from SPIReS, and is characterized by the lowest R value. The CI values are also the

lowest, at around 0.2–0.3 over the TP and most basins. Consequently, MERRA2

505   generates the worst simulation of SCF, both spatially (Section 3.1) and temporally. The

contrast in performance between HMASR and MERRA2, both of which use the same

meteorological forcing (Liu et al., 2021) but differ with regards to snow assimilation,

further emphasizes the significant impact of snow assimilation in the reanalysis SCF

datasets.

510   CRAL shows a similar pattern to MERRA2 with respect to the SCF trends, snowfall,

and temperature. In addition, it also does not assimilate snow observations, resulting in

poor SCF trends. JRA55 performs moderately in simulating the SCF trend, similar to

its performance in simulating the spatial distribution. CFSR exhibits a significant SCF

increase over the northeastern TP, which can be partly explained by increased snowfall

515   and decreased temperatures. This leads to low consistency with SPIReS and lower CI

values, especially for the Inner Tibetan Plateau and the Yellow basin. GLDAS exhibits

a widespread and apparent decrease (increase) in snowfall (temperature) over the

Himalayas, leading to a significant SCF decrease. This trend is opposite to the

observations in SPIReS. As a result, GLDAS shows poor trend simulations over

520   Himalaya-related areas such as the Brahmaputra, Salween, Indus, and Amu Darya

basins. The poor performance of GLDAS with respect to annual variability contrasts

with its good performance with respect to the spatial distribution.
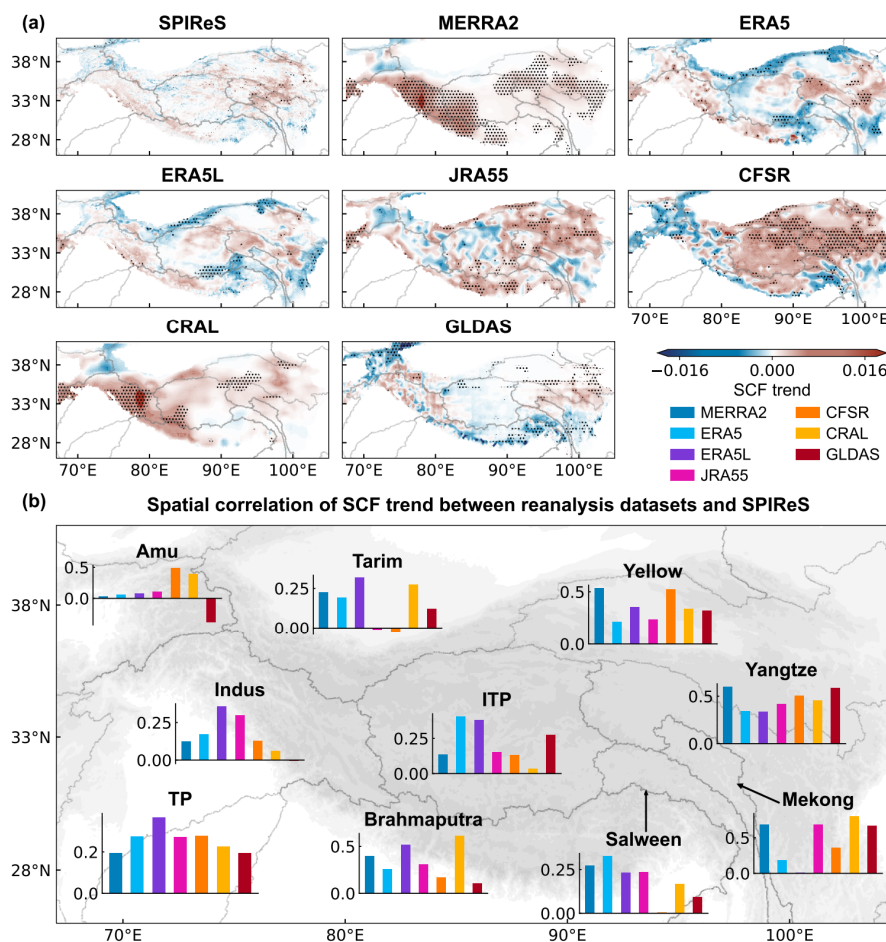
Figure 6: (a) Spatial distribution of the SCF annual trend from the reanalysis datasets over the Tibetan Plateau region over the period 2001 to 2020. (b) Spatial correlations of 20-year SCF trends between the reanalysis datasets and SPIReS in each basin, overlain on a map of the Tibetan Plateau region. Black dots in (a) indicate that the linear trend exceeds the 95% confidence level.
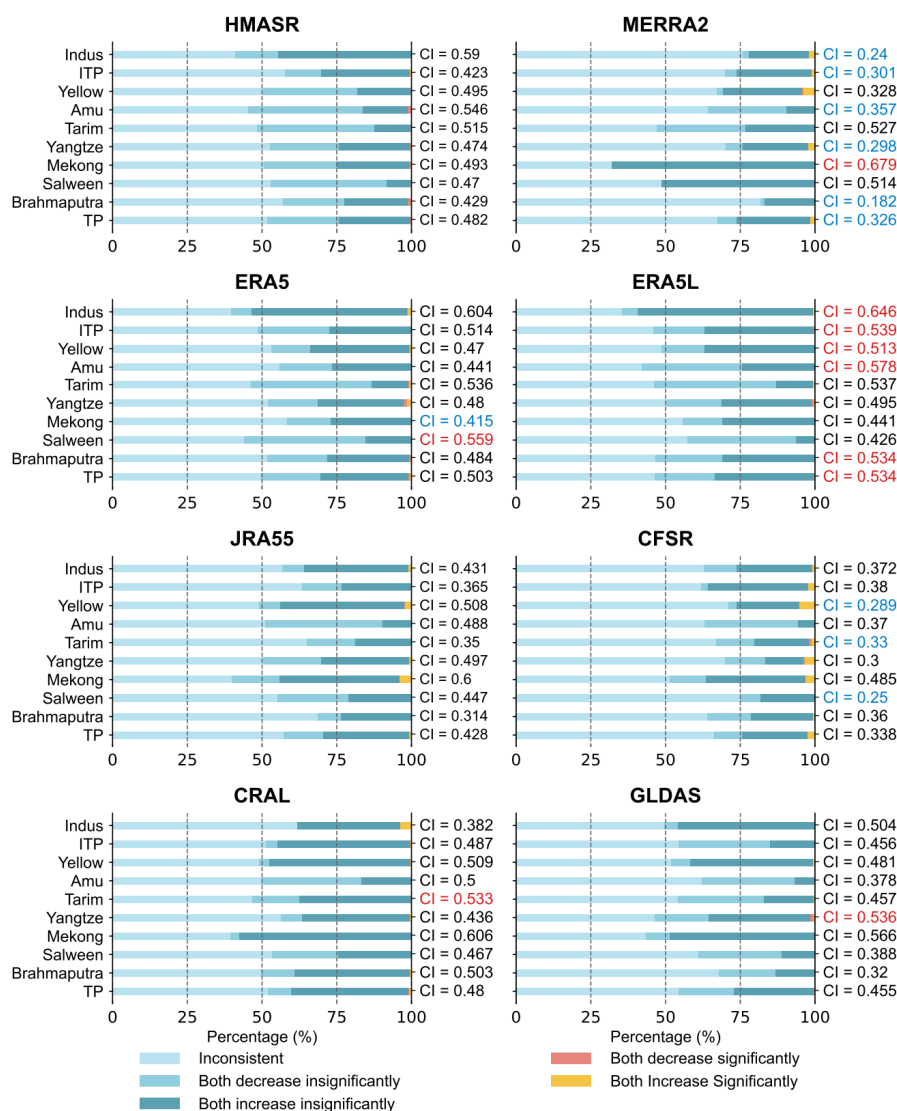
Figure 7: Consistency index (CI) from the reanalysis SCF datasets (excluding HMASR) calculated by comparing with SPIReS dataset trends from 2001 to 2020. The CI value for HMASR was obtained by comparing trends from 2001 to 2016. The red text indicates the maximum CI value within each basin, and the blue text indicates the minimum value.
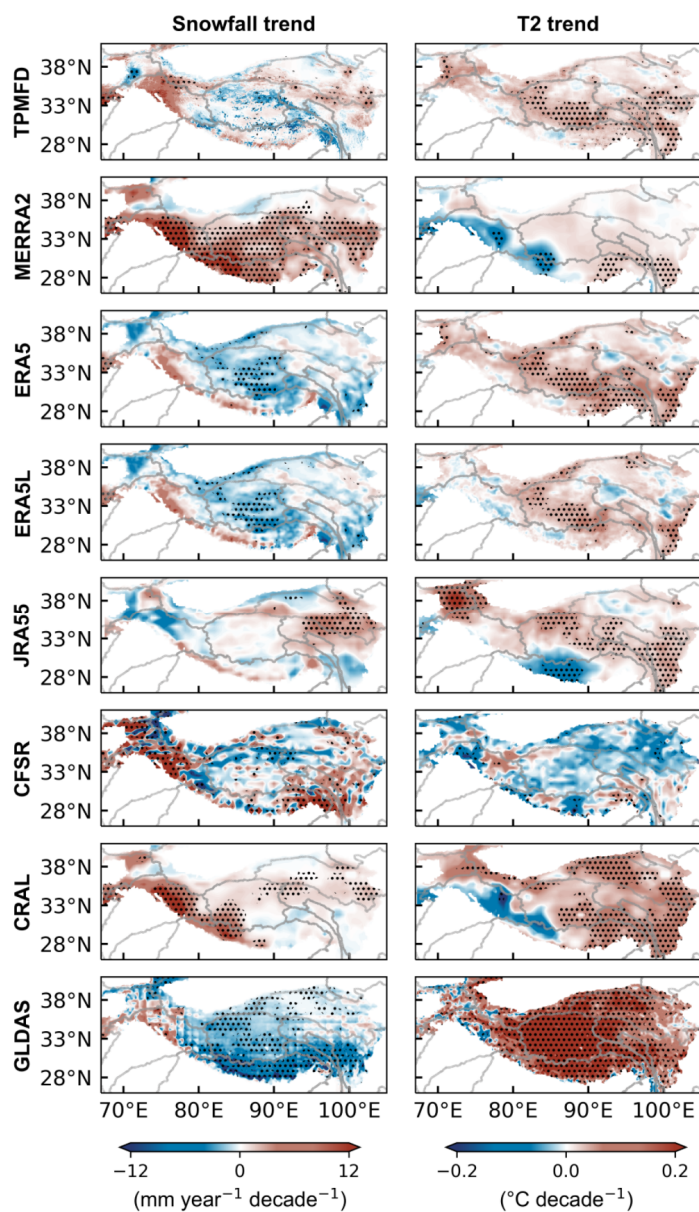
Figure 8: Spatial distribution of the annual snowfall trend over the Tibetan Plateau region for the period 2001 to 2020 from the reanalysis datasets (left), and the T2 annual trend (right). Black dots indicate that the trend exceeds the 95% confidence level.

4 Discussion

4.1 Influence of parameterization method on SCF

For the eight reanalysis datasets analyzed here, five parameterization methods were used to convert SWE or SD into SCF; i.e., MM_SCF, ME_SCF, MJ_SCF, SSiB3_SCF,

545 and Noah_SCF (Section 2.1.2). These parameterization methods have been evaluated in diverse regions (Jiang et al., 2020; Orsolini et al., 2019), and the results indicate that different parameterizations of snow processes will introduce different uncertainties into snow simulations (Jiang et al., 2020). Moreover, specific challenges arise on the TP because of its complex terrain and unstable snow conditions (Huang et al., 2023). In

550 order to evaluate the impact of the parameterization method on SCF simulations and develop an optimized method, we incorporated three parameterization methods (MM_SCF, ME_SCF, and MJ_SCF) separately into each reanalysis dataset to derive another three (two) SCF products for HMASR, CRAL, and CFSR (MERRA2, ERA5, ERA5L, JRA55, and GLDAS). The SSiB3_SCF and Noah_SCF methods were not

555 considered here because their complex schemes cannot be easily applied offline (Ek et al., 2003).

Figure 9 shows the SS and CI values of the SCF simulations from each reanalysis dataset using the different parameterization methods. For most reanalysis datasets, the MM_SCF method generates the best SCF simulation in terms of synthetic performance

560 on spatial and temporal dimensions. This advantage is especially distinct for MERRA2 and ERA5. In addition, MM_SCF is better (more or less) than the built-in method in ERA5, CRAL, and JRA55. These results demonstrate the wide applicability of the MM_SCF method. The performance of ME_SCF is also good, and only slightly below that of MM_SCF. In contrast, MJ_SCF generates the worst SCF simulations for most

565 reanalysis datasets. Even for JRA55, for which MJ_SCF is built-in, the performance is worse than the other two methods, both spatially and temporally. For the SSiB3_SCF

27

and Noah_SCF methods, although they incorporate the complex impacts of the underlying surface characteristics on SCF parameterization, the performance in SCF simulation is only comparable with that of MM_SCF and ME_SCF. This implies that

570 considering the underlying surface characteristics has a limited impact on the accuracy of the SCF simulation. We note that an appropriate parameterization method can actually improve the SCF simulation. However, such improvements do not change the general performance of these eight reanalysis datasets. This indirectly highlights the primary role of meteorological forcing inputs (snowfall and temperature) and snow

575 assimilation with respect to SCF simulations.
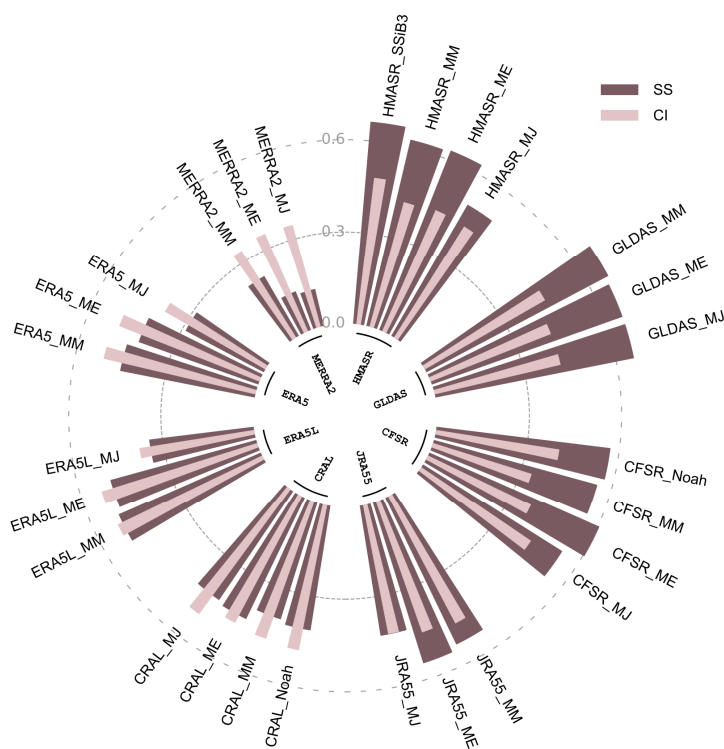
Figure 9: SS and CI values of SCF for all reanalysis datasets calculated offline using the MM_SCF, MJ_SCF, and ME_SCF parameterization methods.

4.2 Reanalysis dataset ensemble for SCF optimization

580   Mortimer et al. (2020) demonstrated that product accuracy can be enhanced by averaging multiple reanalysis datasets, because this allows unrelated errors and deficiencies between them to offset each other. To optimize SCF simulation over the TP, we considered all possible combinations of the eight reanalysis datasets and present the best and worst combinations regarding both the spatial and temporal dimensions

585   (Fig. 10).

Our results reveal that the SCF accuracy does not monotonically improve with the number of combined datasets. For the spatial aspect, the SS value increases from HMASR alone to the combination of HMASR and GLDAS, but then begins to decrease with the continued increasing number of datasets used. Consequently, we concluded

590   that an ensemble of HMASR and GLDAS is optimal for spatial SCF studies over the TP. This implies that the combination of more datasets does not always improve simulation accuracy, and may instead have a negative impact. This appears reasonable because HMASR and GLDAS have excellent accuracy in simulating the spatial variability of SCF, but the addition of poorly performing datasets (e.g., MERRA2 and

595   JRA55) introduces more bias, resulting in a suboptimal outcome. From a temporal aspect, the CI value is highest for the combination of six datasets (i.e., ERA5L, CFSR, CRAL, GLDAS, ERA5, and MERRA2), but is similar when using from three to seven datasets. This differs from the SS result. As these datasets generally demonstrate moderate accuracy in simulating annual SCF trends, a combination of more datasets

600   helps offset the deficiencies within each dataset, leading to an overall enhancement in accuracy. In contrast to the optimal combination, the worst combination shows a monotonically improving performance for both spatial and temporal trends. Notably, each worst combination includes the MERRA2 dataset, whereas HMASR and ERA5L consistently contribute to the optimal combination for SS and CI. This corresponds with

605   the results in Section 3.
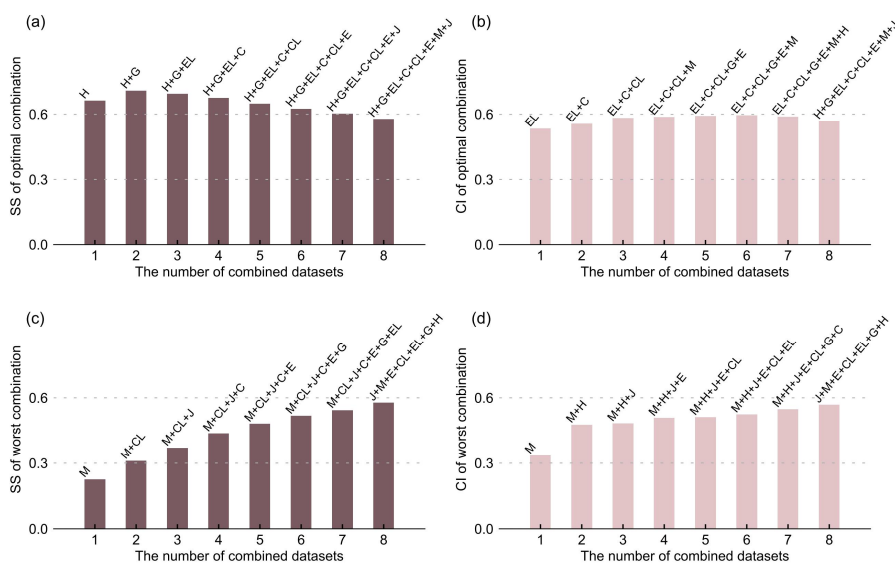
Figure 10: (a) SS for optimal reanalysis dataset combinations across varying numbers of datasets. (b) As in (a) but for CI. (c) and (d) As in (a) and (b), but for the worst combinations.

4.3 Limitations

This study focused primarily on the impact of snowfall and temperature within snow models, as well as snow data assimilation and the choice of SCF parameterization, on the performance of reanalysis datasets in simulating SCF over the TP. However, other model parameters related to precipitation and temperature, such as the precipitation gradient used to describe precipitation variations at different elevations, and the critical temperature used to distinguish rain from snow, are equally vital to snow simulations (Zhang et al., 2015). Furthermore, snow, being a suspended substance, is susceptible to sublimation. It is estimated that blowing snow sublimation accounts for ~30% of global surface sublimation (Déry and Yau, 2002). The TP is perpetually influenced by the westerly jet stream, and processes such as blowing snow sublimation may be significant under windy and arid conditions. However, most LSMs used in reanalysis datasets do not consider blowing snow (Mortimer et al., 2020), and deficiencies in their model

30

structures may also affect the accuracy of SCF simulations.

In addition to these factors, the spatial resolution of reanalysis datasets may also affect

625   the accuracy of SCF simulations. Lei et al. (2023) pointed out that reanalysis datasets characterized by finer spatial resolutions exhibit better consistency with in situ measurements of SD over the TP; e.g., ERA5L outperforms ERA5 and MERRA2. In our study, the fine spatial resolution version of GLDAS generates better SCF simulations than the coarse spatial resolution version for both spatial and temporal

630   dimensions (Fig. S2), which demonstrates the non-negligible impact of model resolution on the accuracy of SCF simulations. This also indirectly implies that the much finer resolution of $1/225° \times 1/225°$ may contribute to the outstanding performance of HMASR. However, SCF products with different spatial resolutions are available only in GLDAS. Therefore, this study cannot conclusively state that the impact of spatial

635   resolution on SCF accuracy is universal.

5. Conclusions

Snow cover on the TP is highly sensitive to climate change. With global climate warming, the quantity and variability of SCF have become crucial indicators for understanding climate change and related hydrological processes. In this study, we

640   assessed the ability and attributed the biases of eight reanalysis datasets to simulate spatiotemporal variations in SCF over the TP based on SPIReS satellite data covering the period 2001–2020. The key findings are:

HMASR exhibits the best accuracy in SCF simulation among all eight reanalysis datasets. Its outstanding performance is benefiting from the snow assimilation of the

645   moderate-resolution MODIS satellite and high-resolution Landsat satellite data, which can improve SCF simulation of the temporal and spatial scales, respectively. GLDAS and CFSR also demonstrate commendable SCF accuracy, comparable to that of HMASR, with CFSR benefiting from snow assimilation. However, CRAL exhibits

650 moderate performance in SCF, and MERRA2 generates the worst SCF simulation both spatially and temporally. The absence of snow assimilation may be responsible for poorer SCF simulations generated by MERRA2 and CRAL, because it uses the same meteorological forcings as HMASR and CFSR.

ERA5 and ERA5L exhibit pronounced SCF overestimations over most TP areas, but the trend simulation is the best in this study. In ERA5 and ERA5L, overestimated
655 snowfall and underestimated temperature jointly contributed to the overestimation of SCF over most of the TP. Moreover, compared with snowfall, temperature-related physical processes have a more pronounced and widespread responsibility for SCF bias and the seasonal variation of SCF bias.

JRA55 similarly overestimates the SCF. We find that SCF accuracy of JRA55 is
660 sensitive to the choice of SCF parameterization, rather than meteorological forcings and snow assimilation.

A two-member ensemble of HMASR and GLDAS was optimal for the study of SCF spatial scales, whereas a six-member ensemble of ERA5L, CFSR, CRAL, GLDAS, ERA5, and MERRA2 was optimal for the study of annual trends.

665 These findings are crucial for selecting the most suitable reanalysis SCF datasets and gaining deeper insights into SCF variations and their controlling mechanisms on the TP. Reducing uncertainties within reanalysis SCF datasets stands as a pivotal stride toward refining climate models and prediction systems. Considering the significant impact of precipitation and temperature bias, along with snow assimilation, acquiring more
670 precise meteorological forcing data and snow observations data is essential to further enhance the accuracy of reanalysis SCF simulations. Simultaneously, selecting more appropriate parameterization methods specific to reanalysis data models will contribute to improving dataset reliability. Optimizing simulations of snow cover on the TP will provide critical support for future climate change research and response strategies.

675

Conflicts of interest

The authors declared that they have no conflicts of interest to this work. We declare that we do not have any commercial or associative interest that represents a conflict of interest in connection with the work submitted.

680

Data Availability Statement

The SPIReS product used in this work is publicly available from http://ftp.snow.ucsb.edu. The TPMFD dataset are obtained from the National Tibetan Plateau Science Data Center (TPDC; https://cstr.cn/18406.11.Atmos.tpdc.300398.). All

685 the reanalysis data are publicly available and can be freely downloaded from the internet.

References

Adler, R.F., Huffman, G.J., Chang, A., Ferraro, R., Xie, P.-P., Janowiak, J., Rudolf, B., Schneider, U.,
695   Curtis, S., Bolvin, D., Gruber, A., Susskind, J., Arkin, P., Nelkin, E., 2003. The Version-2 Global
Precipitation Climatology Project (GPCP) monthly precipitation analysis (1979–present). J.
Hydrometeorol. 4, 1147–1167. https://doi.org/10.1175/1525-
7541(2003)004<1147:TVGPCP>2.0.CO;2

Andreadis, K.M., Lettenmaier, D.P., 2006. Assimilating remotely sensed snow observations into a
700   macroscale hydrology model. Adv. Water Resour. 29, 872–886.
https://doi.org/10.1016/j.advwatres.2005.08.004

Bair, E.H., Stillinger, T., Dozier, J., 2021. Snow Property Inversion from Remote Sensing (SPIReS): a
generalized multispectral unmixing approach with examples from MODIS and Landsat 8 OLI. IEEE
Trans. Geosci. Remote Sens. 59, 7270–7284. https://doi.org/10.1109/TGRS.2020.3040328

705   Beniston, M., Farinotti, D., Stoffel, M., Andreassen, L.M., Coppola, E., Eckert, N., Fantini, A., Giacona,
F., Hauck, C., Huss, M., Huwald, H., Lehning, M., López-Moreno, J.-I., Magnusson, J., Marty, C.,
Morán-Tejéda, E., Morin, S., Naaim, M., Provenzale, A., Rabatel, A., Six, D., Stötter, J., Strasser,
U., Terzago, S., Vincent, C., 2018. The European Mountain cryosphere: a review of its current state,
trends, and future challenges. The Cryosphere 12, 759–794. https://doi.org/10.5194/tc-12-759-2018

710   Bian, Q., Xu, Z., Zhao, L., Zhang, Y.-F., Zheng, H., Shi, C., Zhang, S., Xie, C., Yang, Z.-L., 2019.
Evaluation and intercomparison of multiple snow water equivalent products over the Tibetan
Plateau. J. Hydrometeorol. 20, 2043–2055. https://doi.org/10.1175/JHM-D-19-0011.1

Brown, R.D., Brasnett, B., Robinson, D., 2003. Gridded North American monthly snow depth and snow
water equivalent for GCM evaluation. Atmosphere-Ocean 41, 1–14.
715   https://doi.org/10.3137/ao.410101

Brown, R.D., Mote, P.W., 2009. The response of Northern Hemisphere snow cover to a changing climate*.
J. Clim. 22, 2124–2145. https://doi.org/10.1175/2008JCLI2665.1

Dawson, N., Broxton, P., Zeng, X., Leuthold, M., Barlage, M., Holbrook, P., 2016. An evaluation of snow
initializations in NCEP global and regional forecasting models. J. Hydrometeorol. 17, 1885–1901.

720   https://doi.org/10.1175/JHM-D-15-0227.1

de Rosnay, P., Balsamo, G., Albergel, C., Muñoz-Sabater, J., Isaksen, L., 2014. Initialisation of land surface variables for numerical weather prediction. Surv. Geophys. 35, 607–621. https://doi.org/10.1007/s10712-012-9207-x

Déry, S.J., Yau, M.K., 2002. Large-scale mass balance effects of blowing snow and surface sublimation. J. Geophys. Res. Atmospheres 107, ACL 8-1-ACL 8-17. https://doi.org/10.1029/2001JD001251

Dozier, J., Painter, T.H., Rittger, K., Frew, J.E., 2008. Time–space continuity of daily maps of fractional snow cover and albedo from MODIS. Adv. Water Resour. 31, 1515–1526. https://doi.org/10.1016/j.advwatres.2008.08.011

Dutra, E., Kotlarski, S., Viterbo, P., Balsamo, G., Miranda, P.M.A., Schär, C., Bissolli, P., Jonas, T., 2011. Snow cover sensitivity to horizontal resolution, parameterizations, and atmospheric forcing in a land surface model. J. Geophys. Res. Atmospheres 116. https://doi.org/10.1029/2011JD016061

Ek, M.B., Mitchell, K.E., Lin, Y., Rogers, E., Grunmann, P., Koren, V., Gayno, G., Tarpley, J.D., 2003. Implementation of Noah land surface model advances in the National Centers for Environmental Prediction operational mesoscale Eta model. J. Geophys. Res. Atmospheres 108, 2002JD003296. https://doi.org/10.1029/2002JD003296

Fujiwara, M., Wright, J.S., Manney, G.L., Gray, L.J., Anstey, J., Birner, T., Davis, S., Gerber, E.P., Harvey, V.L., Hegglin, M.I., Homeyer, C.R., Knox, J.A., Krüger, K., Lambert, A., Long, C.S., Martineau, P., Molod, A., Monge-Sanz, B.M., Santee, M.L., Tegtmeier, S., Chabrillat, S., Tan, D.G.H., Jackson, D.R., Polavarapu, S., Compo, G.P., Dragani, R., Ebisuzaki, W., Harada, Y., Kobayashi, C., McCarty, W., Onogi, K., Pawson, S., Simmons, A., Wargan, K., Whitaker, J.S., Zou, C.-Z., 2017. Introduction to the SPARC Reanalysis Intercomparison Project (S-RIP) and overview of the reanalysis systems. Atmos. Chem. Phys. 17, 1417–1452. https://doi.org/10.5194/acp-17-1417-2017

Gelaro, R., McCarty, W., Suárez, M.J., Todling, R., Molod, A., Takacs, L., Randles, C.A., Darmenov, A., Bosilovich, M.G., Reichle, R., Wargan, K., Coy, L., Cullather, R., Draper, C., Akella, S., Buchard, V., Conaty, A., Silva, A.M. da, Gu, W., Kim, G.-K., Koster, R., Lucchesi, R., Merkova, D., Nielsen, J.E., Partyka, G., Pawson, S., Putman, W., Rienecker, M., Schubert, S.D., Sienkiewicz, M., Zhao,

B., 2017. The Modern-Era Retrospective analysis for Research and Applications, version 2 (MERRA-2). J. Clim. 30, 5419–5454. https://doi.org/10.1175/JCLI-D-16-0758.1

Hall, D.K., Riggs, G.A., Salomonson, V.V., DiGirolamo, N.E., Bayr, K.J., 2002. MODIS snow-cover products. Remote Sens. Environ. 83, 181–194. https://doi.org/10.1016/S0034-4257(02)00095-0

Helfrich, S.R., McNamara, D., Ramsay, B.H., Baldwin, T., Kasheta, T., 2007. Enhancements to, and forthcoming developments in the Interactive Multisensor Snow and Ice Mapping System (IMS). Hydrol. Process. 21, 1576–1586. https://doi.org/10.1002/hyp.6720

Hernández-Henríquez, M.A., Déry, S.J., Derksen, C., 2015. Polar amplification and elevation-dependence in trends of Northern Hemisphere snow cover extent, 1971–2014. Environ. Res. Lett. 10, 044010. https://doi.org/10.1088/1748-9326/10/4/044010

Hersbach, H., Bell, B., Berrisford, P., Hirahara, S., Horányi, A., Muñoz-Sabater, J., Nicolas, J., Peubey, C., Radu, R., Schepers, D., Simmons, A., Soci, C., Abdalla, S., Abellan, X., Balsamo, G., Bechtold, P., Biavati, G., Bidlot, J., Bonavita, M., Chiara, G., Dahlgren, P., Dee, D., Diamantakis, M., Dragani, R., Flemming, J., Forbes, R., Fuentes, M., Geer, A., Haimberger, L., Healy, S., Hogan, R.J., Hólm, E., Janisková, M., Keeley, S., Laloyaux, P., Lopez, P., Lupu, C., Radnoti, G., Rosnay, P., Rozum, I., Vamborg, F., Villaume, S., Thépaut, J., 2020. The ERA5 global reanalysis. Q. J. R. Meteorol. Soc. 146, 1999–2049. https://doi.org/10.1002/qj.3803

Huang, J., Zhou, X., Wu, G., Xu, X., Zhao, Q., Liu, Yimin, Duan, A., Xie, Y., Ma, Y., Zhao, P., Yang, S., Yang, K., Yang, H., Bian, J., Fu, Y., Ge, J., Liu, Yuzhi, Wu, Q., Yu, H., Wang, B., Bao, Q., Qie, K., 2023. Global climate impacts of land-surface and atmospheric processes over the Tibetan Plateau. Rev. Geophys. 61, e2022RG000771. https://doi.org/10.1029/2022RG000771

Huffman, G.J., Adler, R.F., Morrissey, M.M., Bolvin, D.T., Curtis, S., Joyce, R., McGavock, B., Susskind, J., 2001. Global precipitation at one-degree daily resolution from multisatellite observations. J. Hydrometeorol. 2, 36–50. https://doi.org/10.1175/1525-7541(2001)002<0036:GPAODD>2.0.CO;2

Immerzeel, W.W., Van Beek, L.P.H., Bierkens, M.F.P., 2010. Climate change will affect the Asian water towers. Science 328, 1382–1385. https://doi.org/10.1126/science.1183188

Jiang, Y., Chen, F., Gao, Y., He, C., Barlage, M., Huang, W., 2020. Assessment of uncertainty sources in

snow cover simulation in the Tibetan Plateau. J. Geophys. Res. Atmospheres 125.

775   https://doi.org/10.1029/2020JD032674

Jiang, Y., Yang, K., Qi, Y., Zhou, X., He, J., Lu, H., Li, Xin, Chen, Y., Li, Xiaodong, Zhou, B., Mamtimin,

A., Shao, C., Ma, X., Tian, J., Zhou, J., 2023. TPHiPr: a long-term (1979–2020) high-accuracy

precipitation dataset (1⁄30°, daily) for the Third Pole region based on high-resolution atmospheric

modeling and dense observations. Earth Syst. Sci. Data 15, 621–638. https://doi.org/10.5194/essd-

780   15-621-2023

Kendall, M.G., 1975. Rank Correlation Methods. J. Inst. Actuar. 75, 140–141.

https://doi.org/10.1017/S0020268100013019

Kitoh, A., Arakawa, O., 2016. Reduction in the east–west contrast in water budget over the Tibetan

Plateau under a future climate. Hydrol. Res. Lett. 10, 113–118. https://doi.org/10.3178/hrl.10.113

785   Koster, R.D., Suarez, M.J., Ducharne, A., Stieglitz, M., Kumar, P., 2000. A catchment-based approach to

modeling land surface processes in a general circulation model: 1. Model structure. J. Geophys. Res.

Atmospheres 105, 24809–24822. https://doi.org/10.1029/2000JD900327

Lei, Y., Pan, J., Xiong, C., Jiang, L., Shi, J., 2023. Snow depth and snow cover over the Tibetan Plateau

observed from space in against ERA5: matters of scale. Clim. Dyn. 60, 1523–1541.

790   https://doi.org/10.1007/s00382-022-06376-0

Li, Q., Yang, T., Li, L., 2022. Evaluation of snow depth and snow cover represented by multiple datasets

over the Tianshan Mountains: Remote sensing, reanalysis, and simulation. Int. J. Climatol. 42,

4223–4239. https://doi.org/10.1002/joc.7459

Liang, X., Jiang, L., Pan, Y., Shi, C., Liu, Z., Zhou, Z., 2020. A 10-Yr global land surface reanalysis

795   interim dataset (CRA-Interim/Land): Implementation and preliminary evaluation. J. Meteorol. Res.

34, 101–116. https://doi.org/10.1007/s13351-020-9083-0

Lin, H., Wu, Z., 2011. Contribution of the autumn Tibetan Plateau snow cover to seasonal prediction of

North American winter temperature. J. Clim. 24, 2801–2813.

https://doi.org/10.1175/2010JCLI3889.1

800   Liu, Y., Fang, Y., Li, D., Margulis, S.A., 2022. How well do global snow products characterize snow

storage in High Mountain Asia? Geophys. Res. Lett. 49. https://doi.org/10.1029/2022GL100082

Liu, Y., Fang, Y., Margulis, S.A., 2021. Spatiotemporal distribution of seasonal snow water equivalent in High Mountain Asia from an 18-year Landsat–MODIS era snow reanalysis dataset. The Cryosphere 15, 5261–5280. https://doi.org/10.5194/tc-15-5261-2021

805 Liu, Z., Jiang, L., Shi, C., Zhang, T., Zhou, Z., Liao, J., Yao, S., Liu, J., Wang, M., Wang, H., Liang, X., Zhang, Z., Yao, Y., Zhu, T., Chen, Z., Xu, W., Cao, L., Jiang, H., Hu, K., 2023. CRA-40/Atmosphere—the first-generation Chinese atmospheric reanalysis (1979–2018): System description and performance evaluation. J. Meteorol. Res. 37, 1–19. https://doi.org/10.1007/s13351-023-2086-x

810 Lyu, M., Wen, M., Wu, Z., 2018. Possible contribution of the inter-annual Tibetan Plateau snow cover variation to the Madden-Julian oscillation convection variability. Int. J. Climatol. 38, 3787–3800. https://doi.org/10.1002/joc.5533

Ma, Y., Ma, W., Zhong, L., Hu, Z., Li, M., Zhu, Z., Han, C., Wang, B., Liu, X., 2017. Monitoring and Modeling the Tibetan Plateau's climate system and its impact on East Asia. Sci. Rep. 7, 44574.
815 https://doi.org/10.1038/srep44574

Magnusson, J., Winstral, A., Stordal, A.S., Essery, R., Jonas, T., 2017. Improving physically based snow simulations by assimilating snow depths using the particle filter. Water Resour. Res. 53, 1125–1143. https://doi.org/10.1002/2016WR019092

Mann, H.B., 1945. Nonparametric tests against trend. Econometrica 13, 245–259.
820 https://doi.org/10.2307/1907187

Meng, J., Yang, R., Wei, H., Ek, M., Gayno, G., Xie, P., Mitchell, K., 2012. The land surface analysis in the NCEP climate forecast system reanalysis. J. Hydrometeorol. 13, 1621–1630. https://doi.org/10.1175/JHM-D-11-090.1

Mortimer, C., Mudryk, L., Derksen, C., Luojus, K., Brown, R., Kelly, R., Tedesco, M., 2020. Evaluation
825 of long-term Northern Hemisphere snow water equivalent products. The Cryosphere 14, 1579–1594. https://doi.org/10.5194/tc-14-1579-2020

Mudryk, L.R., Derksen, C., Kushner, P.J., Brown, R., 2015. Characterization of Northern Hemisphere

snow water equivalent datasets, 1981–2010. J. Clim. 28, 8037–8051. https://doi.org/10.1175/JCLI-D-15-0229.1

830   Muñoz-Sabater, J., Dutra, E., Agustí-Panareda, A., Albergel, C., Arduini, G., Balsamo, G., Boussetta, S., Choulga, M., Harrigan, S., Hersbach, H., Martens, B., Miralles, D.G., Piles, M., Rodríguez-Fernández, N.J., Zsoter, E., Buontempo, C., Thépaut, J.-N., 2021. ERA5-Land: a state-of-the-art global reanalysis dataset for land applications. Earth Syst. Sci. Data 13, 4349–4383. https://doi.org/10.5194/essd-13-4349-2021

835   Onogi, K., Tsutsui, J., Koide, H., Sakamoto, M., Kobayashi, S., Hatsushika, H., Matsumoto, T., Yamazaki, N., Kamahori, H., Takahashi, K., Kadokura, S., Wada, K., Kato, K., Oyama, R., Ose, T., Mannoji, N., Taira, R., 2007. The JRA-25 reanalysis. J. Meteorol. Soc. Jpn. 85, 369–432. https://doi.org/10.2151/jmsj.85.369

Orsolini, Y., Wegmann, M., Dutra, E., Liu, B., Balsamo, G., Yang, K., De Rosnay, P., Zhu, C., Wang, W.,
840   Senan, R., Arduini, G., 2019. Evaluation of snow depth and snow cover over the Tibetan Plateau in global reanalysis using in situ and satellite remote sensing observations. The Cryosphere 13, 2221–2239. https://doi.org/10.5194/tc-13-2221-2019

Painter, T.H., Rittger, K., McKenzie, C., Slaughter, P., Davis, R.E., Dozier, J., 2009. Retrieval of subpixel snow covered area, grain size, and albedo from MODIS. Remote Sens. Environ. 113, 868–879.
845   https://doi.org/10.1016/j.rse.2009.01.001

Qiu, J., 2008. China: The third pole. Nature 454, 393–396. https://doi.org/10.1038/454393a

Reichle, R.H., 2008. Data assimilation methods in the Earth sciences. Adv. Water Resour. 31, 1411–1418. https://doi.org/10.1016/j.advwatres.2008.01.001

Reichle, R.H., Draper, C.S., Liu, Q., Girotto, M., Mahanama, S.P.P., Koster, R.D., Lannoy, G.J.M.D.,
850   2017. Assessment of MERRA-2 Land Surface Hydrology Estimates. J. Clim. 30, 2937–2960. https://doi.org/10.1175/JCLI-D-16-0720.1

Rodell, M., Houser, P.R., Jambor, U., Gottschalck, J., Mitchell, K., Meng, C.-J., Arsenault, K., Cosgrove, B., Radakovich, J., Bosilovich, M., Entin, J.K., Walker, J.P., Lohmann, D., Toll, D., 2004. The global land data assimilation system. Bull. Am. Meteorol. Soc. 85, 381–394.

855   https://doi.org/10.1175/BAMS-85-3-381

Saha, S., Moorthi, S., Pan, H.-L., Wu, X., Wang, Jiande, Nadiga, S., Tripp, P., Kistler, R., Woollen, J.,
        Behringer, D., Liu, H., Stokes, D., Grumbine, R., Gayno, G., Wang, Jun, Hou, Y.-T., Chuang, H.,
        Juang, H.-M.H., Sela, J., Iredell, M., Treadon, R., Kleist, D., Van Delst, P., Keyser, D., Derber, J.,
        Ek, M., Meng, J., Wei, H., Yang, R., Lord, S., Van Den Dool, H., Kumar, A., Wang, W., Long, C.,
860   Chelliah, M., Xue, Y., Huang, B., Schemm, J.-K., Ebisuzaki, W., Lin, R., Xie, P., Chen, M., Zhou,
        S., Higgins, W., Zou, C.-Z., Liu, Q., Chen, Y., Han, Y., Cucurull, L., Reynolds, R.W., Rutledge, G.,
        Goldberg, M., 2010. The NCEP climate forecast system reanalysis. Bull. Am. Meteorol. Soc. 91,
        1015–1058. https://doi.org/10.1175/2010BAMS3001.1

Saha, S., Moorthi, S., Wu, X., Wang, J., Nadiga, S., Tripp, P., Behringer, D., Hou, Y.-T., Chuang, H.,
865   Iredell, M., Ek, M., Meng, J., Yang, R., Mendez, M.P., Van Den Dool, H., Zhang, Q., Wang, W.,
        Chen, M., Becker, E., 2014. The NCEP climate forecast system version 2. J. Clim. 27, 2185–2208.
        https://doi.org/10.1175/JCLI-D-12-00823.1

Sato, N., Sellers, P.J., Randall, D.A., Schneider, E.K., Shukla, J., Kinter, J.L., Hou, Y.-T., Albertazzi, E.,
        1989. Effects of implementing the Simple Biosphere Model in a general circulation model. J.
870   Atmospheric   Sci.   46,   2757–2782.   https://doi.org/10.1175/1520-
        0469(1989)046<2757:EOITSB>2.0.CO;2

Sellers, P.J., Mintz, Y., Sud, Y.C., Dalcher, A., 1986. A Simple Biosphere Model (SIB) for use within
        general   circulation   models.   J.   Atmospheric   Sci.   43,   505–531.   https://doi.org/10.1175/1520-
        0469(1986)043<0505:ASBMFU>2.0.CO;2

875   Sheffield, J., Goteti, G., Wood, E.F., 2006. Development of a 50-Year High-Resolution Global Dataset
        of   Meteorological   Forcings   for   Land   Surface   Modeling.   J.   Clim.   19,   3088–3111.
        https://doi.org/10.1175/JCLI3790.1

Stillinger, T., Rittger, K., Raleigh, M.S., Michell, A., Davis, R.E., Bair, E.H., 2023. Landsat, MODIS,
        and VIIRS snow cover mapping algorithm performance as validated by airborne lidar datasets. The
880   Cryosphere 17, 567–590. https://doi.org/10.5194/tc-17-567-2023

Sun, C., Walker, J.P., Houser, P.R., 2004. A methodology for snow data assimilation in a land surface

model. J. Geophys. Res. Atmospheres 109, 2003JD003765. https://doi.org/10.1029/2003JD003765

Sun, S., Xue, Y., 2001. Implementing a new snow scheme in Simplified Simple Biosphere Model. Adv. Atmospheric Sci. 18, 335–354. https://doi.org/10.1007/BF02919314

885 Taylor, K.E., 2001. Summarizing multiple aspects of model performance in a single diagram. J. Geophys. Res. Atmospheres 106, 7183–7192. https://doi.org/10.1029/2000JD900719

Wang, A., Zeng, X., 2012. Evaluation of multireanalysis products with in situ observations over the Tibetan Plateau. J. Geophys. Res. Atmospheres 117, D05102. https://doi.org/10.1029/2011JD016553

890 Xie, P., Arkin, P.A., 1997. Global precipitation: A 17-year monthly analysis based on gauge observations, satellite estimates, and numerical model Outputs. Bull. Am. Meteorol. Soc. 78, 2539–2558. https://doi.org/10.1175/1520-0477(1997)078<2539:GPAYMA>2.0.CO;2

Xie, P., Chen, M., Yang, S., Yatagai, A., Hayasaka, T., Fukushima, Y., Liu, C., 2007. A gauge-based analysis of daily precipitation over East Asia. J. Hydrometeorol. 8, 607–626.

895 https://doi.org/10.1175/JHM583.1

Xu, W., Ma, L., Ma, M., Zhang, H., Yuan, W., 2017. Spatial–temporal variability of snow cover and depth in the Qinghai–Tibetan Plateau. J. Clim. 30, 1521–1533. https://doi.org/10.1175/JCLI-D-15-0732.1

Xu, X., Lu, C., Shi, X., Gao, S., 2008. World water tower: An atmospheric perspective. Geophys. Res. Lett. 35, L20815. https://doi.org/10.1029/2008GL035867

900 Xue, Y., Sun, S., Kahan, D.S., Jiao, Y., 2003. Impact of parameterizations in snow physics and interface processes on the simulation of snow cover and runoff at several cold region sites. J. Geophys. Res. Atmospheres 108, 2002JD003174. https://doi.org/10.1029/2002JD003174

Yang, K., Jiang, Z., Tang, W., He, J., Shao, C., Zhou, X., Lu, H., Chen, Y., Li, X., Shi, J., 2023. A high-resolution near-surface meteorological forcing dataset for the Third Pole region (TPMFD, 1979-

905 2022). Natl. Tibet. Plateau Data Cent. https://doi.org/10.11888/Atmos.tpdc.300398

You, Q., Wu, F., Wang, H., Jiang, Z., Pepin, N., Kang, S., 2020a. Projected changes in snow water equivalent over the Tibetan Plateau under global warming of 1.5° and 2°C. J. Clim. 33, 5141–5154. https://doi.org/10.1175/JCLI-D-19-0719.1

You, Q., Wu, T., Shen, L., Pepin, N., Zhang, L., Jiang, Z., Wu, Z., Kang, S., AghaKouchak, A., 2020b.

910   Review of snow cover variation over the Tibetan Plateau and its influence on the broad climate

system. Earth-Sci. Rev. 201, 103043. https://doi.org/10.1016/j.earscirev.2019.103043

Yu, L., Zhang, S., Bu, K., Yang, J., Yan, F., Chang, L., 2013. A review on snow data sets. Sci. Geogr. Sin.

33, 878–883. https://doi.org/10.13249/j.cnki.sgs.2013.07.878

Zhang, F., Zhang, H., Hagen, S.C., Ye, M., Wang, D., Gui, D., Zeng, C., Tian, L., Liu, J., 2015. Snow

915   cover and runoff modelling in a high mountain catchment with scarce data: effects of temperature

and precipitation parameters. Hydrol. Process. 29, 52–65. https://doi.org/10.1002/hyp.10125

Zhang, H., Immerzeel, W.W., Zhang, F., De Kok, R.J., Chen, D., Yan, W., 2022. Snow cover persistence

reverses the altitudinal patterns of warming above and below 5000 m on the Tibetan Plateau. Sci.

Total Environ. 803, 149889. https://doi.org/10.1016/j.scitotenv.2021.149889

920   Zhang, H., Zhang, F., Che, T., Yan, W., Ye, M., 2021. Investigating the ability of multiple reanalysis

datasets to simulate snow depth variability over mainland China from 1981 to 2018. J. Clim. 34,

9957–9972. https://doi.org/10.1175/JCLI-D-20-0804.1

Zhang, T., 2005. Influence of the seasonal snow cover on the ground thermal regime: An overview. Rev.

Geophys. 43, RG4002. https://doi.org/10.1029/2004RG000157

925   Zhou, X., Yang, K., Ouyang, L., Wang, Y., Jiang, Y., Li, X., Chen, D., Prein, A., 2021. Added value of

kilometer-scale modeling over the third pole region: a CORDEX-CPTP pilot study. Clim. Dyn. 57,

1673–1687. https://doi.org/10.1007/s00382-021-05653-8